Journal of Materials Chemistry A

RSC Publishing

PAPER

View Article Online
View Journal | View Issue

Cite this: *J. Mater. Chem. A*, 2013, **1**, 14013

Synthesis, conductivity and structural aspects of $Nd_3Zr_2Li_{7-3x}Al_xO_{12}$

M. A. Howard,[a] O. Clemens,[a] K. S. Knight,[b] P. A. Anderson,[a] S. Hafiz,[c] P. M. Panchmatia[c] and P. R. Slater*[a]

Received 16th August 2013
Accepted 3rd October 2013

DOI: 10.1039/c3ta13252h

www.rsc.org/MaterialsA

In this paper we report the synthesis, structure and Li ion conductivity of a new tetragonal garnet phase $Nd_3Zr_2Li_7O_{12}$. In line with other tetragonal garnet systems, the Li is shown to be ordered in the tetrahedral and distorted octahedral sites, and the Li ion conductivity is consequently low. In an effort to improve the ionic conductivity of the parent material, we have also investigated Al doping to reduce the Li content, $Nd_3Zr_2Li_{5.5}Al_{0.5}O_{12}$, and hence introduce disorder on the Li sublattice. This was found to be successful leading to a change in the unit cell symmetry from tetragonal to cubic, and an enhanced Li ion conductivity. Neutron diffraction studies showed that the Al was introduced onto the ideal tetrahedral garnet site, a site preference also supported by the results of computer modelling studies. The effect of moisture on the conductivity of these systems was also examined, showing significant changes at low temperatures consistent with a protonic contribution in humid atmospheres. In line with these observations, computational modelling suggests favourable exchange energy for the Li^+/H^+ exchange process.

Introduction

The recent portable electronics boom has been driven by advances made in Li ion battery technology. This has led to a large amount of interest in the development of new materials with potential for use in such batteries. In terms of the electrolyte, there is growing interest in the development of new solid state electrolyte systems, which offer potential advantages in terms of cell safety and miniaturisation. In this respect, the lithium containing garnets have been attracting significant interest, following initial reports of high Li ion conductivity in such systems by Thangadurai *et al.*[1] These Li containing garnets are unusual in the sense that they show an excess of cations (Li) compared to the traditional garnet materials, which have ideal general formula $A_3B_2C_3O_{12}$ (where the A site is 8 coordinate, the B site is 6 coordinate and the C site is 4 coordinate). Thus in the Li ion conducting garnets, the conventional 8 coordinate (A) and 6 coordinate (B) sites are fully occupied, while partial occupancy of the tetrahedral (C) sites is observed, with additional Li in interstitial distorted octahedral sites not normally occupied in the garnet structure. Thus the stoichiometry of these Li ion conducting garnets can be given as $A_3B_2Li_{3+x}O_{12}$, where $0 \leq x \leq 4$ (ref. 1–14) (the value of x depends on the oxidation states of A and B). The initial work from Thangadurai and Weppner[15] on these systems reported the synthesis of the garnet materials $Li_5La_3M_2O_{12}$ (M = Nb, Ta) with high Li ion conductivities. The authors also reported that it is possible to increase the Li content by partial substitution of the La with K or alkaline earth cations, or by partial substitution of In for Nb.[16] To fully understand the Li ion conductivity of these garnet materials, it is important to have a detailed description of the structure. In this respect, initial structural studies using X-ray diffraction data led to different claims on the location of the Li sites.[17–19] This can be explained by the fact that Li has a weak X-ray scattering factor, which consequently severely hinders its effective location using X-ray diffraction. This problem can be solved through the use of neutron diffraction studies, with initial work in the area by Cussen *et al.* on $Li_5La_3M_2O_{12}$, showing that the space group was $Ia\bar{3}d$, with Li distributed over both the ideal tetrahedral garnet site and also interstitial distorted octahedral sites.[2] Cussen *et al.* also showed that the occupancy of the interstitial sites was only observed for Li contents per formula unit greater than 3, while in systems with ideal conventional garnet stoichiometry, such as $Li_3Ln_3Te_2O_{12}$ (Ln = rare earth), the Li was only present in the tetrahedral site. The Li ion conductivity for $Li_3Nd_3Te_2O_{12}$ system was consequently low ($\sigma_{total(600\ ^\circ C)} = 1 \times 10^{-5}$ S cm^{-1}), and it was concluded that occupancy of both tetrahedral and octahedral sites is the key to ensuring good Li ion conductivity.[14,20]

A number of recent modelling studies have investigated the conduction pathways within these garnet systems. These studies have suggested that the tetrahedral site plays a key role in the conduction pathway of the Li through the structure,[21–23]

[a]School of Chemistry, University of Birmingham, Birmingham, B15 2TT, UK. E-mail: p.r.slater@bham.ac.uk; Fax: +44 (0)121 4144403; Tel: +44 (0)121 4148906
[b]ISIS Facility, Rutherford Appleton Laboratory, Chilton, Oxon, UK
[c]School of Applied Sciences, University of Huddersfield, Huddersfield, HD1 3DH, UK

thus highlighting the need for both Li in the distorted octahedral sites, as well as vacancies in the tetrahedral sites.

Studies aimed at varying the Li content have shown that it is possible to prepare samples with Li contents up to 7 Li per formula unit. In such high Li content garnets, there have been reports of ordering of the Li ions, with 1 Li ion per formula unit located in the garnet tetrahedral site and the remaining 6 Li in the distorted octahedral (4 in the Li2 site, and 2 in the Li3 site) sites, not normally occupied in an ideal stoichiometric garnet.[9] The ordering of the Li atoms within the structure has been reported to be necessary to avoid short Li–Li repulsive interactions. This ordering leads to a tetragonal, rather than cubic, unit cell and a low Li ion conductivity.[9] However, differing results have been observed for the phase with composition $La_3Zr_2Li_7O_{12}$, with reports of both cubic and tetragonal cell symmetry for this system. The formation of cubic systems generally involves high synthesis temperatures (up to 1000 °C) with long heating times (over 12 h), which could give rise to Li_2O evaporation from the system leading to lower than 7 Li per formula unit and hence explaining the cubic unit cell symmetry. Other reports have suggested Al incorporation from reaction with crucibles occurs in these samples, due to the high synthesis temperature. In cases where cubic symmetry has been observed, high Li ionic conductivity was observed (*i.e.* $\sigma_{total(25\ ^\circ C)} \approx 10^{-4}$ S cm^{-1}), while tetragonal samples showed low conductivity due to the ordering of Li. In line with suggestions that Al incorporation from the crucible may be occurring, there have recently been a number of reports of doping on the Li site with Al, Ga, Ge, In and Si.[24–34] Al doping in the $La_3Zr_2Li_7O_{12}$ showed the highest conductivities, of the order of 10^{-4} S cm^{-1} at room temperature.

Another feature of these systems, that has begun to attract attention, is the possibility to partially exchange the Li^+ ions with protons.[35] While many of these studies have focused on exchange through immersion in water, or organic acids, there has been growing interest in the reactivity with moisture from the atmosphere.[36–39] Recently we reported that partial H^+/Li^+ exchange occurs in $La_3Zr_2Ga_{0.5}Li_{5.5}O_{12}$ on exposure to air, and that this partial exchange results in a reduction in grain boundary resistance, and hence an increase in the total conductivity at low temperatures.[29]

While there has been considerable work on doping within $La_3Zr_2Li_7O_{12}$, there have been no reports on the variation of the rare earth cation. To this end, we have examined the effect of varying the rare earth size, and this work showed that it was possible to synthesise $Nd_3Zr_2Li_7O_{12}$, while for smaller rare earths, a garnet phase did not form. In this paper we report the synthesis, structure and ionic conductivity of this new tetragonal phase $Nd_3Zr_2Li_7O_{12}$. In an effort to improve the ionic conductivity, we have also investigated Al doping to reduce Li content and hence change the unit cell symmetry from tetragonal to cubic. The characterisation of this Al doped material is also reported, and we also investigate the effect of exposure of the samples to moisture. The experimental work is supported by computational modelling studies into the most favourable dopant position and the energetics behind H^+/Li^+ exchange, the first such studies on these garnet systems.

Experimental

$Nd_3Zr_2Li_7O_{12}$ and $Nd_3Zr_2Li_{5.5}Al_{0.5}O_{12}$ were prepared *via* solid state reactions as follows. Stoichiometric amounts of Nd_2O_3 (99.99% purity), ZrO_2 (99% purity), Al_2O_3 (99% purity), Li_2CO_3 (99% purity) powders (with a 10% molar excess of Li_2CO_3, to account for Li_2O loss by chemical transport with traces of water yielding volatile LiOH) were ground together in an agate pestle and mortar until a homogeneous powder was achieved. The powder was transferred into an alumina crucible and then heated at 600 °C for 2 hours. The temperature was then increased to 800 °C for 12 hours. The heated powder was removed from the furnace and reground with a further 10% molar excess Li_2CO_3 added. The powder was then pressed into a pellet and the pellet was heated at temperatures of 850 °C for 12 hours for $Nd_3Zr_2Li_7O_{12}$, and 1000 °C for 4 hours for $Nd_3Zr_2Li_{5.5}Al_{0.5}O_{12}$. The garnet pellets were placed on zirconia pellets to avoid any Al incorporation from the crucible at the elevated reaction temperature. X-ray diffraction (Bruker D8 diffractometer with Cu Kα_1 radiation) was used to determine phase purity.

For conductivity measurements, pellets were pressed and heated at different temperatures and times (up 1200 °C for 1–12 hours, on zirconia pellets to avoid Al incorporation) to examine the effect of sintering temperature on the conductivity. It was found that heating for 4 hours at 1000 °C gave a density of ~82% of the crystallographic density. Higher temperature heat treatment led to the formation of significant perovskite-type impurities, attributed to Li loss, and so the sintering temperature was limited to 1000 °C. Ag electrodes were attached to the pellet using Ag paste and the pellet fired again, at 120 °C for 30 min, to give a good electrical contact between the electrode and sample. Conductivity measurements were carried out using A.C. impedance spectroscopy (Hewlett Packard 4192A Impedance Analyser) in the range from 0.1 to 10^3 kHz. Conductivity measurements were performed in wet and dry N_2 to elucidate any changes in the conductivity on exposure to moisture. In order to confirm that the conductivity changes in wet atmospheres were not simply due to surface conduction along the edges of the pellet, impedance spectra were also collected on a pellet where the lateral pellet surfaces were covered with silicon-based grease (Dow corning high vacuum grease). In these experiments electrodes were applied to the pellet with the inner circle removed to create a ring-shaped electrode (shown in Fig. 1). This experimental approach allows for water incorporation into the sample, while preventing surface conduction: such an approach was demonstrated previously by Mather *et al.* in the study of proton conduction in nano-crystalline YSZ,[40] where the authors showed that in this case the enhanced conductivity in wet atmosphere was due to surface conduction rather than bulk effects. Impedance data were analysed using ZView software[41] by fitting the data to appropriate equivalent circuits.

Neutron diffraction data for $Nd_3Zr_2Li_7O_{12}$ and $Nd_3Zr_2Li_{5.5}Al_{0.5}O_{12}$ were collected on the HRPD diffractometer, ISIS, Rutherford Appleton Laboratory. All structure refinements used the Topas suite of Rietveld refinement software.[42]

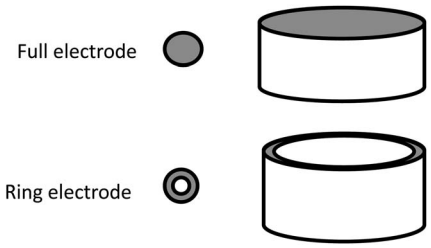

Fig. 1 Diagram illustrating ring-shaped electrode and standard electrode arrangements for conductivity measurements.

Computational methods

In this study, well established atomistic modelling methods embodied in the GULP code[44] have been used, and these methods have been reviewed elsewhere.[45,46] The calculations are based on the Born model for polar solids where the interactions between ions are represented in terms of a long-range Coulombic term plus an analytical function representing short-range repulsive and van der Waals interactions. For this study, the short-range interactions were modelled using the Buckingham potential:

$$V_{ij}(r) = A_{ij}\exp\left(\frac{-r}{\rho_{ij}}\right) - \frac{c_{ij}}{r^6} \quad (1)$$

where r is the interatomic distance and A, ρ and C are empirically derived parameters. Charged defects will polarise nearby ions in the lattice and therefore, to calculate the defect energies accurately, we included the electronic polarisability in the model, which is incorporated *via* the shell model.[47] Point defects were modelled using the Mott–Littleton approach, in which a defect is introduced into the energy-minimised lattice, and the surrounding ions partitioned into two regions.[47,48] An inner sphere of ions immediately surrounding the point defect (region 1) is then relaxed explicitly whilst the crystal bulk (region 2) is treated by computationally less expensive quasi-continuum methods.

As with previous modelling studies on protons in perovskite oxides[49] and silicate minerals[50,51] the OH interaction was treated using an attractive Morse potential (with Coulomb subtraction):

$$V(r) - D\{1 - \exp[-\beta(r - r_0)]\}^2 \quad (2)$$

Table 1 Interatomic Buckingham potentials and shell model parameters for $Nd_3Zr_2Li_7O_{12}$ and $Nd_3Zr_2Li_{5.5}Al_{0.5}O_{12}$

Interaction	A (eV)	ρ (Å)	C (eV Å^6)	γ (e)	k (eV Å^{-2})
$Li^+\cdots O^{2-}$	292.3000	0.3472	0.0000	1.00	99 999
$Zr^{4+}\cdots O^{2-}$	985.8690	0.3670	0.0000	1.35	169.92
$Nd^{3+}\cdots O^{2-}$	1995.2000	0.3430	22.5900	3.00	99 999
$Al^{3+}\cdots O^{2-}$	1142.6775	0.2991	0.0000	3.00	99 999
$O^{2-}\cdots O^{2-}$	22764.30	0.1490	43.0000	−2.86	74.92
$H^+\cdots O^{2-a}$	311.9700	0.2500	0.0000	—	—

[a] Morse intra-molecular parameters: D = 7.0525 eV; β = 2.1986 Å^{-1}; r_o = 0.9485 Å; charge O core: −1.4263, H core: +0.4263.

using parameters (listed in Table 1) developed from *ab initio* quantum mechanical cluster calculations,[50] with a point charge representation of the surrounding lattice. The dipole moment of the OH group was simulated by placing charges of −1.4263 and +0.4263 on the O and H species, respectively (overall charge −1.00) in accordance with this study. Additional Buckingham parameters were employed to simulate the interaction of the lattice oxygen atoms with the hydroxyl unit.[50,51] Lattice energies for the binary oxides required in the doping studies were calculated using the parameters listed in Table 1, whilst a correction term was added to account for the change in chemical potential energy due to the formation of LiOH and Li_2CO_3 from Li_2O using the following equations:

$$Li_2O + H_2O \rightarrow 2LiOH \quad (3)$$

$$Li_2O + CO_2 \rightarrow Li_2CO_3 \quad (4)$$

The correction term was calculated using experimental enthalpy of formation at 300 K.[52,53]

Results

Structural studies

X-ray diffraction patterns showed that the $Nd_3Zr_2Li_7O_{12}$ garnet phase was successfully prepared, with peak splitting indicative of a tetragonal unit cell. In contrast the Al doped phase, $Nd_3Zr_2Li_{5.5}Al_{0.5}O_{12}$, showed a simpler X-ray diffraction pattern, consistent with a cubic unit cell (Fig. 2). This change in symmetry is an indication that Al has been successfully doped onto one of the 3 Li sites, leading to the creation of 2 Li^+ vacancies for each Al^{3+} introduced (one Al^{3+} will replace three Li^+), and hence allowing the introduction of disorder and the change in the symmetry to a cubic unit cell.

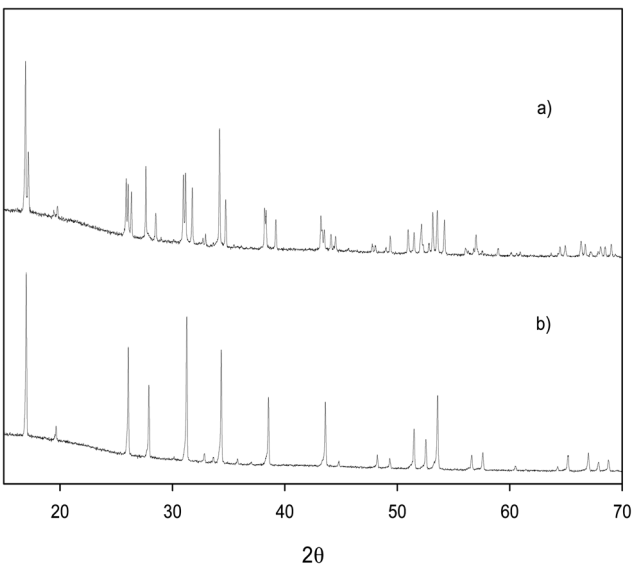

Fig. 2 X-ray diffraction patterns for (a) $Nd_3Zr_2Li_7O_{12}$ and (b) $Nd_3Zr_2Li_{5.5}Al_{0.5}O_{12}$.

Table 2 Structural parameters for $Nd_3Zr_2Li_7O_{12}$ from neutron powder diffraction data[a]

Atom	Site	*x*	*y*	*z*	Fractional occupancy
Nd1	8b	0	1/4	1/8	1
Nd2	16e	0.1271(1)	0	1/4	1
Zr	16c	0	0	0	1
Li1	8a	0	1/4	3/8	1
Li2	16f	0.1819(4)	0.4319(4)	1/8	1
Li3	32g	0.0803(4)	0.0885(4)	0.8042(4)	1
O1	32g	0.2773(1)	0.0986(1)	0.1949(1)	1
O2	32g	0.1945(1)	0.2834(1)	0.0971(1)	1
O3	32g	0.1012(1)	0.1942(1)	0.2828(1)	1

[a] Tetragonal, $I4_1/acd$, $a = 12.94711(9)$, $c = 12.5512(1)$ Å, $B_{iso,eq} = 0.25(1)$, $R_{wp} = 3.580$, $R_{exp} = 1.152$, GOF = 3.107.

Neutron diffraction data were analysed to determine the location of the Al in $Nd_3Zr_2Li_{5.5}Al_{0.5}O_{12}$, as well as the Li positions and distribution in both this and the parent $Nd_3Zr_2Li_7O_{12}$ phase. For the latter, the structure of the tetragonal garnet phase $La_3Zr_2Li_7O_{12}$ (ref. 43) with space group $I4_1/acd$, was used as an initial starting model (where La ions were replaced by Nd ions). In the refinement an empirical absorption correction was included to account for absorption from the Li and Nd in the samples (this was included in both refinements). The structure refinement confirmed the tetragonal symmetry, with cell parameters of $a = 12.9471(1)$ Å, $c = 12.5511(1)$ Å. When comparing the unit cell parameters of previously reported tetragonal $La_3Zr_2Li_7O_{12}$ with tetragonal $Nd_3Zr_2Li_7O_{12}$, a decrease in unit cell size is observed with the Nd sample, which is as expected due to the smaller size of Nd^{3+} (1.109 Å, 8 coordinate) compared to La^{3+} (1.160 Å, 8 coordinate).[54] Atomic positions were refined for $Nd_3Zr_2Li_7O_{12}$ and gave sensible values with low positional errors for the respective sites. Li occupancies were initially set at full occupancy for each site. Refinement of these Li site occupancies led to negligible change from full occupancy. The values were therefore fixed at full occupancy for the final refinement. Refinement of the atomic displacement parameters led to values with large errors, and so an overall parameter for the phase was refined. Some extra peaks were present in the neutron diffraction pattern, which could be attributed to Li_2CO_3 from the excess used in the synthesis, and the vanadium sample can used in the experiment. These were included in the refinement as secondary phases. The final structural parameters and bond distances are presented in Tables 2 and 3, with the observed, calculated and difference neutron diffraction profiles presented in Fig. 3.

In the Rietveld refinement of the structure of $Nd_3Zr_2Al_{0.5}Li_{5.5}O_{12}$, the structural model for $La_3Nb_2Li_5O_{12}$ with space group $Ia\bar{3}d$ (ref. 2) was used as a starting point, again with the replacement of La by Nd. This confirmed the cubic cell with unit cell parameters of $a = 12.8158(1)$ Å. In the first instance, it was assumed that only Li was present on the Li sites, and the occupancies of these sites were allowed to vary in the refinement. From this refinement, the occupancy of the Li1 (24d) (ideal tetrahedral) site showed a value close to zero. As Li has a negative scattering length and Al has a positive scattering length this was a good indication that Al had been successfully doped onto this site. The Al on the Li1 (24d) site was therefore added to the refinement and the occupancy of the Al was fixed at the value (1/6) expected from the initial sample composition. The occupancy of this site by Al was supported by the modelling

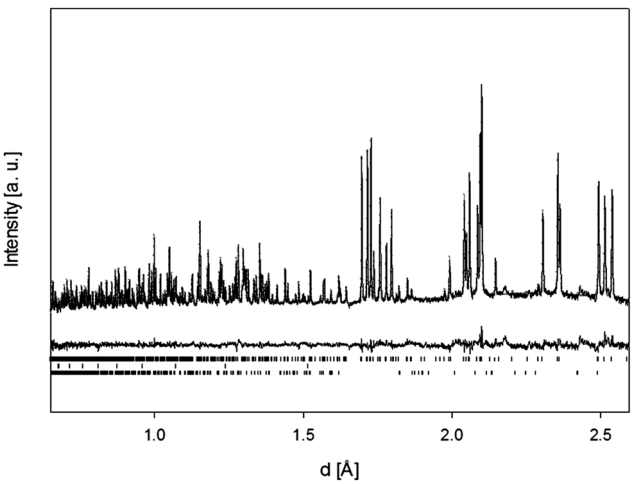

Fig. 3 The observed, calculated and difference neutron diffraction data profiles for $Nd_3Zr_2Li_7O_{12}$ (lower tick marks Li_2CO_3, middle tick marks vanadium sample can, upper tick marks $Nd_3Zr_2Li_7O_{12}$).

Table 3 Selected bond distances for $Nd_3Zr_2Li_7O_{12}$ from neutron diffraction studies, along with calculated mean bond lengths from modelling studies

Bond	Experimental bond distance	Calculated mean bond distance	Bond	Experimental bond distance	Calculated mean bond distance
Nd1–O1 [x2]	2.426(2)	2.433	Li2–O2 [x2]	1.968(6)	1.974
Nd1–O1 [x2]	2.497(2)	2.468	Li2–O1 [x2]	2.349(2)	2.342
Nd1–O2 [x2]	2.518(2)	2.536	Li2–O1 [x2]	2.379(7)	2.552
Nd1–O3 [x2]	2.568(2)	2.621	Li3–O1	1.852(6)	1.848
Nd2–O3 [x4]	2.484(2)	2.488	Li3–O2	2.035(7)	2.055
Nd2–O2 [x4]	2.580(2)	2.643	Li3–O2	2.049(7)	2.159
Zr–O2 [x2]	2.094(2)	1.975	Li3–O3	2.195(6)	2.263
Zr–O3 [x2]	2.102(2)	1.997	Li3–O3	2.719(6)	2.749
Zr–O1 [x2]	2.107(2)	2.011	Li3–O3	2.834(7)	2.919
Li1–O3 [x4]	1.889(2)	1.964			

Table 4 Structural parameters for $Nd_3Zr_2Li_{5.5}Al_{0.5}O_{12}$ from neutron powder diffraction data[a]

Atom	Site	x	y	z	Fractional occupancy
Nd1	24c	1/8	0	1/4	1
Zr1	16a	0	0	0	1
Li1	24d	3/8	0	1/4	0.35(2)
Li2	96h	0.103(1)	0.687(1)	0.574(1)	0.368(5)
Al1	24d	3/8	0	1/4	1/6
O1	96h	0.2808(1)	0.0984(1)	0.1945(1)	1

[a] Cubic, $Ia\bar{3}d$, $a = 12.8158(1)$ Å, $B_{iso,eq} = 0.32(2)$, $R_{wp} = 4.828$, $R_{exp} = 1.527$, GOF = 3.162.

studies (see next section). The Li occupancies were then constrained to equal 5.5 Li atoms per formula unit, again as expected from the sample stoichiometry. The fractional Li occupancies were then refined, giving the tetrahedral Li1 (24d) site a Li occupancy of 0.35(2) and the distorted octahedral site Li2 (96h) an occupancy of 0.368(5). Refinement of the Li3 (highly distorted octahedral) site (found to be occupied in other Li containing garnets) led to zero occupancy of this site, and so this site was removed from the refinement. As with the refinement of the structure of tetragonal $Nd_3Zr_2Li_7O_{12}$, an overall atomic displacement parameter was refined.

As before, extra peaks were observed due to the vanadium sample can which was included as a secondary phase. Final structural parameters and bond distances are presented in Tables 4 and 5. The observed, calculated and difference neutron diffraction profiles are presented in Fig. 4.

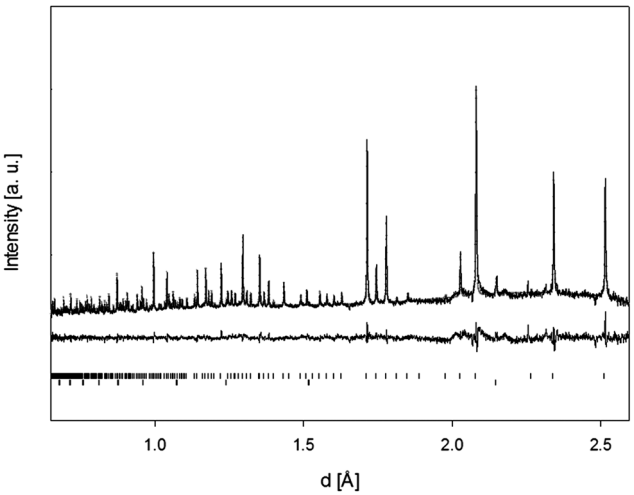

Fig. 4 The observed, calculated and difference neutron diffraction data profiles for $Nd_3Zr_2Li_{5.5}Al_{0.5}O_{12}$ (lower tick marks vanadium sample can, upper tick marks $Nd_3Zr_2Li_{5.5}Al_{0.5}O_{12}$).

Modelling studies

The interatomic potentials used for the modelling studies of $Nd_3Zr_2Li_7O_{12}$ and $Nd_3Zr_2Li_{5.5}Al_{0.5}O_{12}$ are listed in Table 1, while Table 6 shows the structural reproduction of the calculated structure, illustrating a fit to within 1% of the observed cell parameters. This represents excellent agreement especially since the modelling of these structures is not trivial given their complex nature, with Li present in both the tetrahedral and octahedral coordination sites. Fig. 5(a) and (b) show the schematic representations of both the tetragonal and cubic structures. Tables 3 and 5 list the experimental and mean calculated bond lengths for $Nd_3Zr_2Li_7O_{12}$ and $Nd_3Zr_2Al_{0.5}Li_{5.5}O_{12}$ respectively. Following the successful reproduction of the structures, defect modelling and dopant solution energies were calculated, the latter to include both trivalent cation doping on the Li sites, and H^+/Li^+ exchange.

The defect modelling suggests the most favourable intrinsic defect to be the Li Frenkel defect, see Table 7. The dopant studies in $Nd_3Zr_2Li_7O_{12}$ suggest the Li1 (tetrahedral) site to be the most favoured site for Al doping in accord with the diffraction studies. The local structural analysis from

Table 6 Structural comparisons (experimental and calculated) for (a) $Nd_3Zr_2Li_7O_{12}$ and (b) $Nd_3Zr_2Li_{5.5}Al_{0.5}O_{12}$

Parameter	Experimental	Calculated	Difference (% diff.)
(a) $Nd_3Zr_2Li_7O_{12}$			
a/Å	12.9471	12.9674	0.01993(0.15)
b/Å	12.9471	12.9674	0.0199(0.15)
c/Å	12.5512	12.5864	0.0353(0.28)
$\alpha = \beta = \gamma$	90.0	90.0	0.0(0.00)
(b) $Nd_3Zr_2Li_{5.5}Al_{0.5}O_{12}$			
a/Å	12.8158	12.8246	0.0088(0.07)
b/Å	12.8158	12.8179	0.0021(0.02)
c/Å	12.8158	12.8126	−0.0032(−0.03)
$\alpha = \beta = \gamma$	90.0	90.0	0.0(0.00)

Table 5 Selected bond distances for $Nd_3Zr_2Li_{5.5}Al_{0.5}O_{12}$ from neutron diffraction studies, along with calculated mean bond lengths from modelling studies

Bond	Experimental bond distance	Calculated mean bond distance	Bond	Bond distance	Calculated mean bond distance
Nd–O [x4]	2.469(2)	2.425	Li2–O	1.875(17)	1.937
Nd–O [x4]	2.545(2)	2.549	Li2–O	2.128(18)	2.020
Zr–O [x6]	2.110(2)	2.073	Li2–O	2.144(16)	2.109
Li1–O [x4]	1.881(2)	1.926	Li2–O	2.194(18)	2.219
Al–O[x4]	1.881(2)	1.662	Li2–O	2.518(17)	2.435
			Li2–O	2.657(16)	2.659

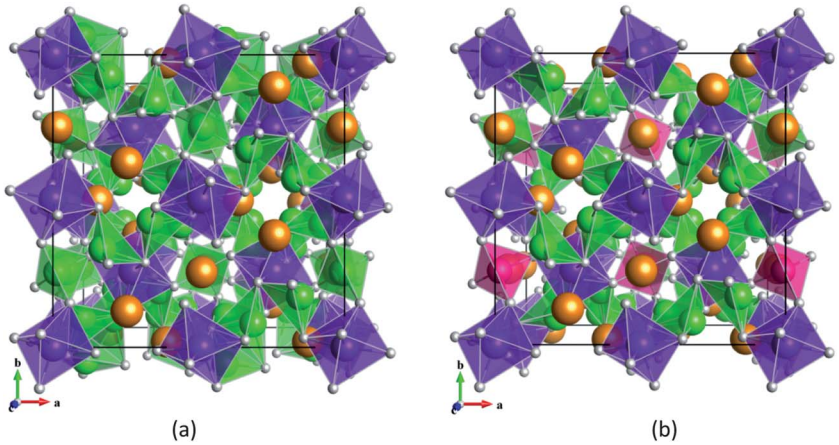

Fig. 5 Schematic representation of the structures of (a) $Nd_3Zr_2Li_7O_{12}$ and (b) $Nd_3Zr_2Li_{5.5}Al_{0.5}O_{12}$. Key: Nd – orange; Zr – purple; Li – green; O – grey; Al – pink.

the simulations indicates shorter Al–O bond lengths compared to the Li–O equivalents in the $Nd_3Zr_2Li_7O_{12}$. The Al is closer to its nearest neighbour Li3 (octahedral site) by 0.25 Å than the Li1–Li3 distance in the non-doped tetragonal structure. This might indicate why the Li3 site is not occupied by Li for the Al doped cubic sample, since this would lead to unfavourable strong cation–cation repulsion. The results also show that the nearest neighbour Li, that used to be in the octahedral coordination site, has a tendency to displace to achieve LiO_4 tetrahedral coordination, see Fig. 6(a). The next nearest lithium however remains octahedrally coordinated suggesting no long-range distortions. A similar situation is also observed for the $Nd_3Zr_2Li_{5.5}Al_{0.5}O_{12}$ phase. From these calculations Al doping on the Li sites is predicted to be favourable in accord with experimental observations.

In determining the trivalent dopant solution energies, three different mechanisms were investigated (equations shown in Table 8), where Li_2O, Li_2CO_3 and LiOH were possible by-products of the doping studies. Table 8 lists the most favourable calculated solution energies for doping a variety of trivalent atoms (Al, Ga, In) in place of Li. These M^{3+} dopants were predicted to favour the tetrahedral Li1 site. The modelling also implies that if CO_2 is present, then the formation of Li_2CO_3 is most favourable. The results therefore suggests that the atmosphere (*i.e.* partial pressures of H_2O, CO_2) used in the synthesis may have an effect on the incorporation of dopants in these garnet systems. In addition to the analysis of the incorporation of trivalent dopants, modelling of Li^+/H^+ exchange has also been investigated. Table 8 lists the two mechanisms considered for proton-exchange. The solution energies for proton exchange imply that the formation of Li_2CO_3 is more favourable than the formation of LiOH as a by-product, suggesting again that the atmosphere, which the sample is exposed to, may have a significant effect on this process. Local structure analysis of the proton environment suggests that the H^+ prefers to exchange with the Li on the octahedral site causing significant distortions as it forms a typical O–H bond (0.978 Å) with the nearest neighbour oxygen (illustrated in Fig. 6(b)). Neighbouring octahedral and tetrahedral Li sites are also slightly distorted. Local atomic distances are shown in Fig. 6(b).

Conductivity studies

Room temperature A.C. impedance measurements of $Nd_3Zr_2Li_7O_{12}$ in wet and dry N_2 recorded a very high resistance at the limit of the instrument capability. At higher temperatures, an increase in the conductivity was observed, but the conductivity remained low consistent with the ordered nature of the Li ion distribution in this phase. Arrhenius plots comparing the conductivity of the sample in wet and dry N_2 are presented in Fig. 7. A small improvement in the bulk conductivity was observed in wet N_2 experiments in the temperature range 100–400 °C. Activation energies were calculated to be 0.55 eV in wet N_2 atmosphere and 0.66 eV for the dry N_2 experiments. This improvement in the conductivity can be attributed to the effect of H^+/Li^+ exchange, which would lead to a number of consequences. The introduction of protons may lead to a protonic contribution to the conductivity, while the

Table 7 Intrinsic defects

$Nd_3Zr_2Li_7O_{12}$

Defects	Defect equations	Energy (eV)
Li Frenkel	$Li_{Li}^{\times} \rightarrow V'_{Li} + Li_i^{\cdot}$	0.78
O Frenkel	$O_O^{\times} \rightarrow V_O^{\cdot\cdot} + O_i''$	6.52
Schottky	$2Zr_{Zr}^{\times} + 12O_O^{\times} + 3Nd_{Nd}^{\times} + 7Li_{Li}^{\times} \rightarrow 2V''''_{Zr} + 12V_O^{\cdot\cdot} + 3V'''_{Nd} + 7V'_{Li} + Nd_3Li_7Zr_2O_{12}$	31.69

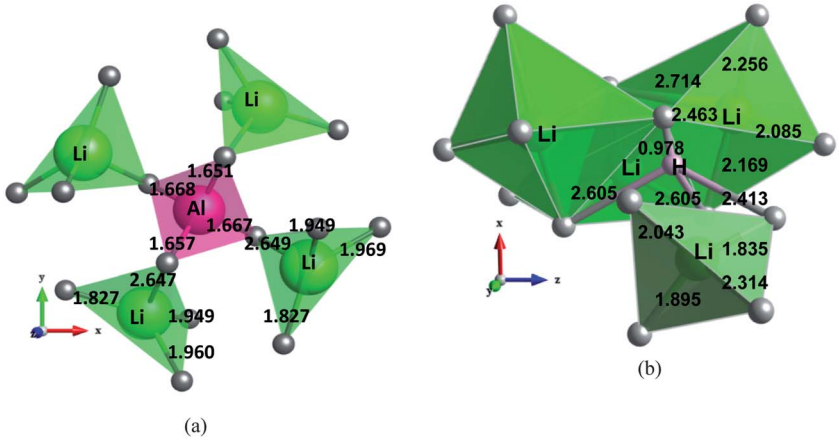

Fig. 6 Local structure of the (a) Al site where the most favourable doping site is the Li tetrahedral site, and (b) H site where the most favourable doping site was the Li octahedral site. All the distances are in ångströms. Key: Li – green and blue; O – grey; Al – pink; H – white.

Table 8 M^{3+} and H^{+} doping mechanism equations and energies

$M_2O_3 + 6Li_{Li}^{\times} \rightarrow 2M_{Li}^{\cdot\cdot} + 4V_{Li}' + 3Li_2O$	(1)
$M_2O_3 + 6Li_{Li}^{\times} + 3CO_2 \rightarrow 2M_{Li}^{\cdot\cdot} + 4V_{Li}' + 3Li_2CO_3$	(2)
$M_2O_3 + 6Li_{Li}^{\times} + 3H_2O \rightarrow 2M_{Li}^{\cdot\cdot} + 4V_{Li}' + 6LiOH$	(3)
$H_2O + Li_{Li}^{\times} \rightarrow H_{Li}^{\times} + LiOH$	(4)
$H_2O + CO_2 + 2Li_{Li}^{\times} \rightarrow 2H_{Li}^{\times} + Li_2CO_3$	(5)

$Nd_3Zr_2Li_7O_{12}$

Dopant	Bond lengths	Energy (eV)
Al–O x4	1.662	0.113 (eqn (1))
		−2.172 (eqn (2))
		−1.890 (eqn (3))
Ga–O x4	1.854	3.505 (eqn (1))
		1.220 (eqn (2))
		1.501 (eqn (3))
In–O x4	1.980	3.810 (eqn (1))
		1.525 (eqn (2))
		1.807 (eqn (3))
H–O	0.978	−0.977 (eqn (4))
		−2.703 (eqn (5))

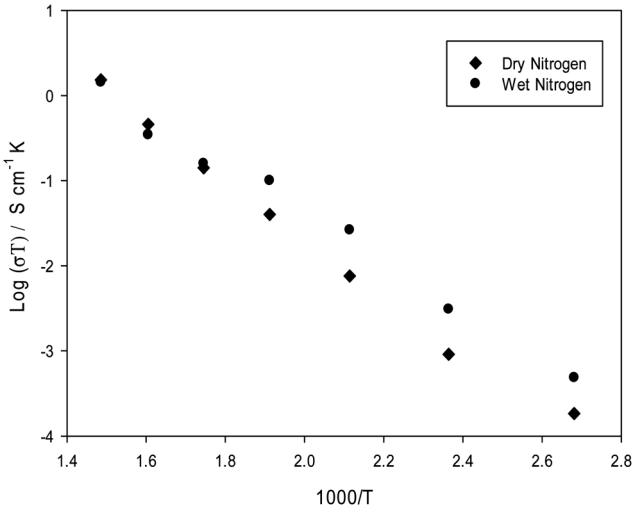

Fig. 7 Arrhenius plots of bulk conductivity for $Nd_3Zr_2Li_7O_{12}$ in wet N_2, and dry N_2, showing an enhancement for the latter at low temperatures.

creation of Li ion vacancies may increase the Li ion conductivity. The H^+/Li^+ exchange may also lead to a partial suppression of the local Li ordering, which could also account for the improved conductivity. In this respect, a recent study by Larraz *et al.* has shown that proton incorporation in the related $La_3Zr_2Li_7O_{12}$ can lead to a change from an ordered tetragonal system to a disordered cubic system.[55]

Room temperature A.C. impedance measurements for $Nd_3Zr_2Al_{0.5}Li_{5.5}O_{12}$ showed significantly higher conductivities, as expected from the introduction of Al lowering the Li content, and hence leading to disorder on the Li sublattice. Under a wet N_2 atmosphere, the impedance spectrum at RT showed a single semi-circle which was characteristic of a bulk response (Fig. 8). The conductivity was calculated to be $\sigma_{bulk(25\ ^\circ C)} = 3.9 \times 10^{-5}$ S cm^{-1}, comparable to values previously reported for other cubic Li ion conducting garnets. The activation energy was calculated to be 0.56 eV between 100 and 400 °C. For the dry N_2 atmosphere, the room temperature data showed a larger bulk semicircle, along with the beginning of a second feature attributed to a grain boundary response (Fig. 9). The bulk conductivity was calculated to be $\sigma_{bulk(25\ ^\circ C)} = 9.1 \times 10^{-6}$ S cm^{-1}, indicating a lower bulk conductivity than in the wet atmosphere. At higher temperatures, both the data in dry and wet N_2 showed the presence of two semicircles consistent with bulk and grain boundary components. Equivalent circuits were used to fit these data and are presented in Fig. 10 and 11 for the 100 °C data set. The activation energy was calculated to be 0.38 eV in the dry N_2 atmosphere between 100 and 400 °C, which is slightly lower than for the wet N_2 data.

Arrhenius plots comparing the conductivities in wet N_2 and dry N_2 are shown in Fig. 12. These data show interesting variations. In particular, at temperatures below 100 °C, the bulk conductivity is lower in dry N_2 than in wet N_2, suggesting an additional protonic contribution in the latter. However, at

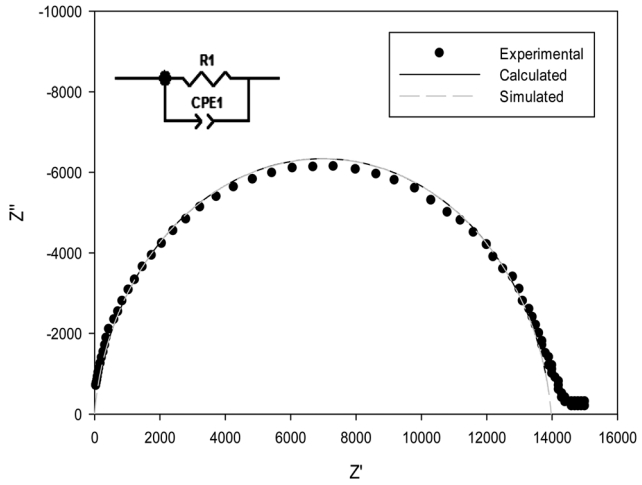

Fig. 8 Observed (circle), calculated (black line), simulated (grey dashed line) Nyquist plot at room temperature in wet N_2 for $Nd_3Zr_2Li_{5.5}Al_{0.5}O_{12}$.

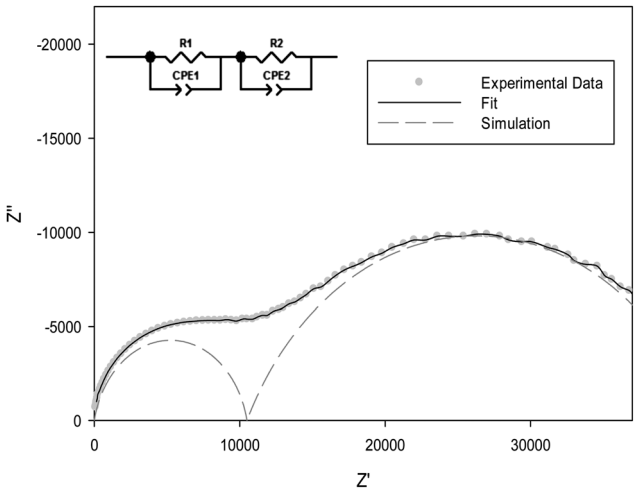

Fig. 10 Experimental (circle), fit (grey line) and simulated (dashed line) profiles for wet N_2 A.C. impedance measurements at 100 °C for $Nd_3Zr_2Li_{5.5}Al_{0.5}O_{12}$.

100 °C and above, the conductivity in dry N_2 becomes higher. The higher bulk conductivity at the temperatures above 100 °C in dry N_2 is consistent with prior studies of $La_3Zr_2Ga_{0.5}Li_{5.5}O_{12}$, where the effect of H^+/Li^+ exchange was to reduce the bulk conductivity, while enhancing the grain boundary conductivity. A similar enhancement of the grain boundary conductivity was observed for $Nd_3Zr_2Al_{0.5}Li_{5.5}O_{12}$. In this case, however, there also appears to be an enhancement in the bulk conductivity below 100 °C. It was thought that this may be related to surface conduction; recent work suggesting high room temperature proton conductivity in nano-crystalline yttria-stabilised zirconia[40] has been similarly identified as being due to surface conduction. In order to determine whether surface conduction was also a factor in the case of these garnet materials, A.C. impedance measurements were recorded on pellets, which had been coated with silicone grease on the lateral surface (as described in the experimental section; see Fig. 1). In wet N_2, the impedance spectrum (Fig. 13) showed a similar reduced bulk resistance compared to the dry N_2 experiment. (Note: the increase in resistance compared to the initial wet N_2 data set is due to the fact that in this experiment, the inner circle of Ag has been removed to create a ring-shaped electrode, leading to a reduction in the electrode area.) The fact that the conductivity is still enhanced in this experiment could be taken suggest that there is bulk rather than surface proton conduction, although given the fact that the pellet was only ~82% dense, it is not possible to discount water incorporation into the pores and resultant surface conduction along grains (as noted in the experimental section, attempts to increase the pellet density by higher temperature sintering led to significant Li loss). Possible support for the enhancement being due to bulk conduction is, however, provided by recent results by Larraz *et al.*, who have reported the presence of bulk water at low temperatures in garnet Li ion conductors.[55] Such water insertion would increase

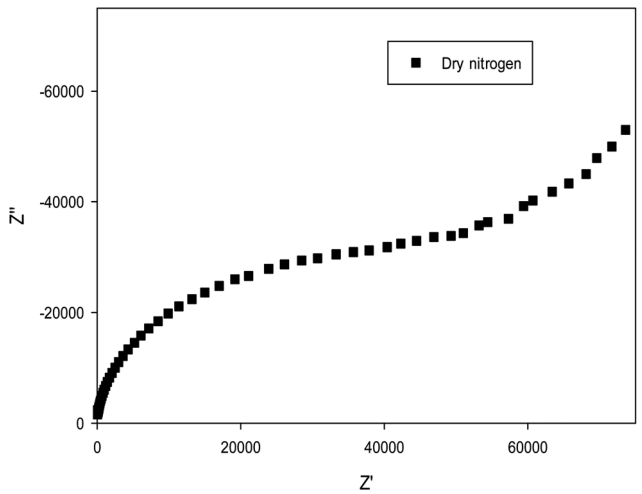

Fig. 9 Observed Nyquist plot at room temperature in dry N_2 for $Nd_3Zr_2Li_{5.5}Al_{0.5}O_{12}$.

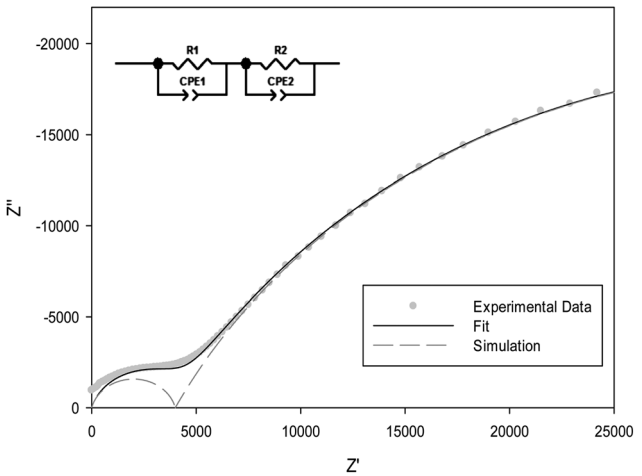

Fig. 11 Experimental (circle), fit (grey line) and simulated (dashed line) profiles for dry N_2 A.C. impedance measurements at 100 °C for $Nd_3Zr_2Li_{5.5}Al_{0.5}O_{12}$.

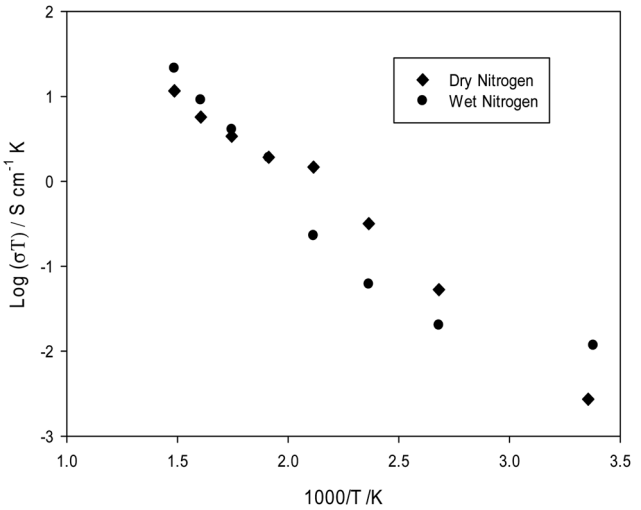

Fig. 12 Arrhenius plots of bulk conductivity for $Nd_3Zr_2Al_{0.5}Li_{5.5}O_{12}$ in wet N_2, and dry N_2.

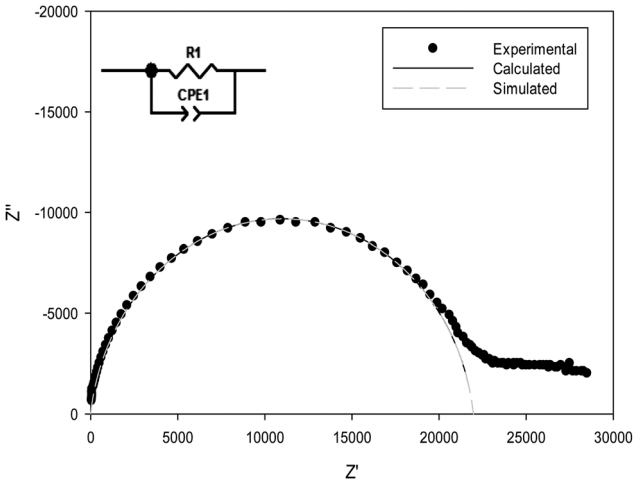

Fig. 13 Observed (circle), calculated (black line), simulated (grey dashed line) Nyquist plot for ring shaped electrode experiment at room temperature in wet N_2 for $Nd_3Zr_2Li_{5.5}Al_{0.5}O_{12}$.

the H content and so may enhance the protonic contribution to conduction leading to the observed conductivity enhancement. The results therefore suggest further work on the effect of water on these garnet materials is warranted. In particular there is a need for the preparation and analysis of dense pellets through low temperature/short heating time routes, *e.g.* spark plasma sintering, to avoid Li loss.

Conclusions

We have shown the successful synthesis of the tetragonal garnet phase $Nd_3Zr_2Li_7O_{12}$ for the first time. We have also shown that it is possible to change the unit cell symmetry to cubic by doping on the Li sites with Al. Neutron diffraction studies were used to determine that Al had been doped onto the ideal garnet tetrahedral site, also supported by the results of modelling studies. Conductivity measurements of the tetragonal $Nd_3Zr_2Li_7O_{12}$ sample showed low conductivity due to Li ordering. Doping with Al improved the conductivity *via* creating defects within the structure. It was shown that, in both samples, moisture has a significant effect on the conductivity. The elimination of the grain boundary component in wet atmospheres is especially significant, with regard to the total conductivity, and shows that care should be taken to ensure elimination of water in assessing the room temperature Li ion conductivity of these systems. The modelling studies further support the favourability of the Li^+/H^+ exchange process, with the favoured H^+ site being the distorted octahedral Li site. The modelling studies also suggest that the atmosphere may also have an effect on the degree of exchange.

Acknowledgements

We would like to thank the Engineering and Physical Sciences Research Council (EPSRC) and the University of Birmingham for financial support (studentship for MH). Neutron diffraction beamtime at ISIS, Rutherford Appleton Lab, was provided by the Science and Technology Facilities Council (STFC). The Bruker D8 used in this research were obtained through the Science City Advanced Materials project, with support from Advantage West Midlands (AWM) and part funded by the European Regional Development Fund (ERDF). O. Clemens would like to thank the German Academic Exchange Service (DAAD) for providing a postdoctoral fellowship. P. M. Panchmatia would like to thank Dr David J. Cooke, University of Huddersfield, for useful discussions on the doping mechanisms. P. M. P. would like to acknowledge membership of the UK's HPC Materials Chemistry Consortium, which is funded by EPSRC (Grant No. EP/F067496) and the use of the University of Huddersfield Queensgate Grid in carrying out this work.

References

1 V. Thangadurai, S. Adams and W. Weppner, *Chem. Mater.*, 2004, **16**, 2998.
2 E. J. Cussen, *Chem. Commun.*, 2006, 412.
3 M. P. O'Callaghan and E. J. Cussen, *Chem. Commun.*, 2007, 2048.
4 M. P. O'Callaghan, D. R. Lynham, E. J. Cussen and G. Z. Chen, *Chem. Mater.*, 2006, **18**, 4681.
5 J. Percival and P. R. Slater, *Solid State Commun.*, 2007, **142**, 355.
6 J. Percival, D. Apperley and P. R. Slater, *Solid State Ionics*, 2008, **179**, 1693.
7 J. Percival, E. Kendrick and P. R. Slater, *Solid State Ionics*, 2008, **179**, 1666.
8 J. Percival, E. Kendrick and P. R. Slater, *Mater. Res. Bull.*, 2008, **43**, 765.
9 J. Percival, E. Kendrick, R. I. Smith and P. R. Slater, *Dalton Trans.*, 2009, 5177.
10 J. Awaka, N. Kijima, Y. Takahashi, H. Hayakawa and J. Akimoto, *Solid State Ionics*, 2009, **180**, 602.
11 J. Awaka, N. Kijima, K. Kataoka, H. Hayakawa, K.-i. Ohshima and J. Akimoto, *J. Solid State Chem.*, 2010, **183**, 180.
12 S. Narayanan and V. Thangadurai, *J. Power Sources*, 2011, **196**, 8085.

13 S. K. S. Ohta, J. Seki, T. Saeki, S. Morishita and T. Asaoka, *J. Power Sources*, 2013, 53.
14 E. J. Cussen, *J. Mater. Chem.*, 2010, **20**, 5167.
15 V. Thangadurai, H. Kaack and W. J. F. Weppner, *J. Am. Ceram. Soc.*, 2003, **86**, 437.
16 V. Thangadurai and W. Weppner, *J. Solid State Chem.*, 2006, **179**, 974.
17 D. Mazza, *Mater. Lett.*, 1988, **7**, 205.
18 H. Hyooma and K. Hayashi, *Mater. Res. Bull.*, 1988, **23**, 1399.
19 V. Thangadurai, S. Adams and W. Weppner, *Chem. Mater.*, 2004, **16**, 2998.
20 E. J. Cussen, T. W. S. Yip, G. O'Neill and M. P. O'Callaghan, *J. Solid State Chem.*, 2011, **184**, 470.
21 M. Xu, M. S. Park, J. M. Lee, T. Y. Kim, Y. S. Park and E. Ma, *Phys. Rev. B: Condens. Matter Mater. Phys.*, 2012, **85**, 052301.
22 J. Han, J. Zhu, Y. Li, X. Yu, S. Wang, G. Wu, H. Xie, S. C. Vogel, F. Izumi, K. Momma, Y. Kawamura, Y. Huang, J. B. Goodenough and Y. Zhao, *Chem. Commun.*, 2012, **48**, 9840.
23 R. Jalem, Y. Yamamoto, H. Shiiba, M. Nakayama, H. Munakata, T. Kasuga and K. Kanamura, *Chem. Mater.*, 2013, **25**, 425.
24 M. Huang, A. Dumon and C.-W. Nan, *Electrochem. Commun.*, 2012, **21**, 62.
25 J. Wolfenstine, J. Ratchford, E. Rangasamy, J. Sakamoto and J. L. Allen, *Mater. Chem. Phys.*, 2012, **134**, 571.
26 J. L. Allen, J. Wolfenstine, E. Rangasamy and J. Sakamoto, *J. Power Sources*, 2012, **206**, 315.
27 J. Wolfenstine, J. Sakamoto and J. L. Allen, *J. Mater. Sci.*, 2012, **47**, 4428.
28 E. Rangasamy, J. Wolfenstine and J. Sakamoto, *Solid State Ionics*, 2012, **206**, 28.
29 M. A. Howard, O. Clemens, E. Kendrick, K. S. Knight, D. C. Apperley, P. A. Anderson and P. R. Slater, *Dalton Trans.*, 2012, **41**, 12048.
30 A. Kuhn, J.-Y. Choi, L. Robben, F. Tietz, M. Wilkening and P. Heitjans, *Z. Phys. Chem.*, 2012, **226**, 525.
31 S. Kumazaki, Y. Iriyama, K.-H. Kim, R. Murugan, K. Tanabe, K. Yamamoto, T. Hirayama and Z. Ogumi, *Electrochem. Commun.*, 2011, **13**, 509.
32 H. Buschmann, J. Doelle, S. Berendts, A. Kuhn, P. Bottke, M. Wilkening, P. Heitjans, A. Senyshyn, H. Ehrenberg, A. Lotnyk, V. Duppel, L. Kienle and J. Janek, *Phys. Chem. Chem. Phys.*, 2011, **13**, 19378.
33 A. Duevel, A. Kuhn, L. Robben, M. Wilkening and P. Heitjans, *J. Phys. Chem. C*, 2012, **116**, 15192.
34 H. Buschmann, S. Berendts, B. Mogwitz and J. Janek, *J. Power Sources*, 2012, **206**, 236.
35 T. Lina and V. Thangadurai, *Inorg. Chem.*, 2012, **51**, 1222.
36 L. Truong, M. Howard, O. Clemens, K. S. Knight, P. R. Slater and V. Thangadurai, *J. Mater. Chem. A*, 2013, DOI: 10.1039/c3ta13005c.
37 S. Narayanan, F. Ramezanipour and V. Thangadurai, *J. Phys. Chem. C*, 2012, **116**, 20154.
38 C. Galven, J. Dittmer, E. Suard, F. Le Berre and M. P. Crosnier-Lopez, *Chem. Mater.*, 2012, **24**, 3335.
39 S. Toda, K. Ishiguro, Y. Shimonishi, A. Hirano, Y. Takeda, O. Yamamoto and N. Imanishi, *Solid State Ionics*, 2013, **233**, 102.
40 C. Tande, D. Perez-Coll and G. C. Mather, *J. Mater. Chem.*, 2012, **22**, 11208.
41 D. Johnson, *ZView: a Software Program for IES Analysis 2.8*, 2008.
42 A. Coelho, *Topas Academic v4.1 Computer Software*, Brisbane, 2007.
43 J. Awaka, N. Kijima, H. Hayakawa and J. Akimoto, *J. Solid State Chem.*, 2009, **182**, 2046.
44 J. D. Gale, *J. Chem. Soc., Faraday Trans.*, 1997, **93**, 629.
45 C. R. A. Catlow, *Solid State Chemistry-Techniques*, Clarendon Press, Oxford, 1987.
46 C. R. A. Catlow, *Computer Modelling in Inorganic Crystallography*, Academic Press, San Diego, 1997, p. 340.
47 B. Dick and A. Overhauser, *Phys. Rev.*, 1958, **112**, 90.
48 N. F. Mott and M. J. Littleton, *Trans. Faraday Soc.*, 1938, **34**, 485.
49 (*a*) F. M. Higgins, N. H. de Leeuw and S. C. Parker, *J. Mater. Chem.*, 2002, **12**, 124; (*b*) D. W. Lewis, C. R. A. Catlow and J. M. Thomas, *Faraday Discuss.*, 1997, **106**, 451.
50 K. Wright and C. R. A. Catlow, *Phys. Chem. Miner.*, 1994, **20**, 515.
51 (*a*) A. Gatzemeier and K. Wright, *Phys. Chem. Miner.*, 2006, **33**, 115; (*b*) P. M. Panchmatia, A. Orera, E. Kendrick, J. V. Hanna, M. E. Smith, P. R. Slater and M. S. Islam, *J. Mater. Chem.*, 2010, **20**, 2766.
52 I. Barin and O. Knacke, *Thermochemical Properties of Inorganic Substances*, Springer-Verlag, Berlin, 1973.
53 Y. S. Touloukian and T. Makita, *Thermophysical properties of Matter*, IFI/Plenum, New York, 1970, vol. 6.
54 R. D. Shannon, *Acta Crystallogr., Sect. A: Cryst. Phys., Diffr., Theor. Gen. Crystallogr.*, 1976, **32**, 751.
55 G. Larraz, A. Orera and M. L. Sanjuan, *J. Mater. Chem.*, 2013, **1**, 11419.